

Design a *J*-type air-based battery thermal management system through surrogate-based optimization

Yuanzhi Liu, Jie Zhang*

The University of Texas at Dallas, Richardson, TX 75080, USA

HIGHLIGHTS

- A *J*-type air-based battery thermal management system (BTMS) is proposed.
- Surrogate-based optimization is performed to improve *J*-type BTMS design.
- Results are cross validated between simulations and experiments.

ARTICLE INFO

Keywords:

Thermal management
Electro-thermal model
J-type structure
Surrogate-based optimization

ABSTRACT

Battery thermal management system is of great importance to the performance and safety of electric vehicles. The conventional *U*- and *Z*-type air-based structures may fail to meet the thermal requirements under changing working conditions. This paper proposes a novel *J*-type air-based battery thermal management system by integrating the *U*-type and *Z*-type structures. A comparative parametric study of key design variables and priori optimized structures is first conducted with a newly developed battery electro-thermal model. Based on the parametric analyses, the grouped-channel optimizations are performed using surrogate-based optimization. Results show that there are 35.3%, 46.6%, and 31.18% reduction in temperature rise for *U*-, *Z*-, and *J*-type, respectively. The pros and cons of the *J*-type structure are further explored by comparing with the optimal *U*- and *Z*-type structures. A further *J*-type optimization regarding the manifold configuration is also conducted to show that the optimal settings of the air-based cooling system vary across working conditions, and the *J*-type structure is able to be adaptively controlled to satisfy the cooling requirement. Corresponding experiments are also conducted to validate the modeling and optimization results.

1. Introduction

Electric vehicles (EVs) are likely to flourish in the near future after a rapid development in the past decade. Several major automobile manufacturers have added EVs into their short-term portfolio as a response to the growing movements to cut down vehicle emissions. As the only power source for EVs, in retrospect, the traction battery technologies that have been utilized in EVs industry have progressed from low energy density, i.e., lead-acid, nickel-cadmium, nickel-zinc, and nickel metal hydride battery, to high energy density like lithium-ion battery [1]. The emergence and widely use of lithium-ion battery (LIB) has promoted the rapid development of EVs to a great extent due to its excellent properties, such as high energy density, low self-charging, and low maintenance [2].

Due to the intrinsic properties of lithium-based electrode material [3], the operating temperature is known to have a significant impact on

lithium-ion battery in terms of safety, degradation, and performance. The optimum operating temperature is suggested to be strictly controlled within a narrow range in the literature, i.e., 15–35 °C [4], 25–45 °C [5], and 20–45 °C [6]. It is found that a low temperature tends to increase the internal resistance and lead to capacity deficiencies, while an extremely high temperature may accelerate the electrode degradation and capacity reduction or even safety issues such as fire and explosion [7]. A battery thermal management system (BTMS) is then necessary to maintain the battery thermal surroundings, thereby preventing potential safety risks.

1.1. Review of battery thermal management system

A significant amount of work has been conducted in the literature on the design and evaluation of advanced battery thermal systems. Most of the existing work emphasizes the cooling aspect, while the

* Corresponding author.

E-mail address: jiezhang@utdallas.edu (J. Zhang).

studies of heating aspect have rarely been reported in the literature [8]. State-of-the-art BTMS cooling technologies include active liquid cooling [9], active air cooling, heat pipe, phase change material (PCM) [10], and hybrid approaches of those technologies [11]. The applications of BTMS in EVs industry differ across the distinctions of lithium-ion battery specifications and EVs' positioning, and only air and fluid cooling technologies have been successfully applied in EVs industry, as summarized in Appendix A.

Compared with other thermal management systems, air-based BTMS has been widely employed in EVs industry due to its remarkable advantages like lightweight, simple structure, and low cost. Most of the compact size EVs only have passive air cooling as a trade-off between vehicle weight and cruising capacity, so does the plug-in hybrid electric vehicles (PHEV) powered by lithium iron phosphate (LFP) battery with more stable thermal characteristics. For example, Nissan Leaf and BYD Song have successfully updated for several generations, and the passive cooling systems have been proved to be reliable. PHEV with lithium nickel manganese cobalt Oxide (NMC) battery like Toyota Prius normally employs a fan-driven active air cooling system, since NMC battery is more temperature sensitive than LFP battery in daily operation [12].

However, these applications also reveal the inadequacy of air-based BTMS like non-uniform and limited heat dissipation capability, contamination from external cooling air, and potential noise or vibration. The majority of the existing literature on active pure air-based BTMS focuses on structure design improvement and flow optimization, attempting to uniformize the internal temperature profile of the battery pack. Several general structures of pure air-based BTMS have been proposed in the literature. For example, Park [13] proposed and compared a Z-type and a U-type air-based BTMS with simulations, and found that the thermal requirement can be achieved by changing the tapered manifolds and pressure for both types. Mahamud et al. [14] developed a reciprocating air-based structure that could change straight-through air flow direction with two flip door valves. The numerical results showed that the reciprocating flow can reduce the battery pack temperature difference by 72%. Xun et al. [15] investigated the effects of counterflow arrangement with computational fluid dynamics (CFD) simulations, and suggested that changing the counterflow arrangement and direction periodically might enhance the thermal performance. Wang et al. [16] investigated the impacts of fan location by using both numerical simulation and experiment, and summarized that the top fan location coupled with cubic arrangement was most desired to improve the cooling effects. Yang et al. [17] assessed the series-parallel mixed cooling with aligned bank, staggered bank, and trapezoid configuration for cylindrical lithium-ion battery packs. Shahid et al. [18] examined the effects of multiple vortex generators with experiments, and the results yielded a smaller temperature rise and a higher temperature uniformity. There hasn't been any study to comprehensively compare the pros and cons of all the proposed structures.

Furthermore, the flow efficiency and thermal performance of a specific air-based BTMS structure can be optimized simultaneously with respect to the existing flow field, e.g., the channel interspacing size and the manifold configuration. Chen et al. [19] developed a flow network model to calculate the channel velocity and employed the Newton method to redistribute the air flow rate, in which the simulation results showed a 45% reduction in the maximum temperature difference after optimization. Li et al. [20] examined the parametric effects of a U-type BTMS and optimized the channel flow rate via CFD simulations and flow formulation iterations. Wang et al. [21] proposed to employ a surrogate-based multidisciplinary optimization method to optimize the structure design of an air-based BTMS, and found that the thermal performance and battery lifetime could be improved via structure optimization.

Pure air-based BTMS may encounter challenges under intense or instantaneous working conditions like extreme fast charging and rapid

acceleration, due to its limited thermal conductivity [22]. Based on the specific heat difference between air and other medium, different studies have tried to develop a hybrid cooling system by adding an extra intermediate medium as a thermal buffer in between the battery cells and the cooling air. For instance, a mixed phase changing material (PCM) system can be integrated with passive air cooling, in which additional material can be added to the main PCM (paraffin for most cases) to enhance the thermal conductivity, such as metal foams [23], graphene, expanded graphite [24], and graphite of nanocomposite structure [25]. It is also reported that a PCM system coupled with forced air cooling can yield a more desired performance than pure PCM or pure forced convective air cooling, especially after a long time operation [26]. Moreover, a hybrid heat pipe cooling system coupled with forced air ventilation can effectively control the temperature to be evenly distributed under abusive discharging conditions [27]. Note that none of these studies have been reported to be successfully integrated into industrial EV applications due to their complexity and instability.

1.2. Research motivation and objective

All the air-based cooling technologies discussed above have already been proven to have the capability of well controlling the battery temperature in an appropriate range. Compared with the hybrid air-based BTMS, pure air cooling has incomparable advantages in terms of stability, maintenance, and vehicle power-to-weight ratio. Existing air cooling systems attempt to modify the configurations of the channel and manifold to uniformize air flow rate with a lower pressure drop so as to enhance the temperature uniformity and energy efficiency simultaneously. However, It is challenging to achieve these goals with the conventional U- or Z-type BTMS with a fixed structure under changing working conditions (e.g., discharging, charging, extreme fast charging, etc.), especially for large battery packs. To address this challenge, this paper proposes a flexible air cooling structure, named J-type, emerging from the existing Z- and U-type. The proposed J-type BTMS has two outlets with control valves, which adds more cooling flexibility to the BTMS under varying battery working conditions. By controlling the opening degree of the two valves simultaneously, the J-type BTMS can be adaptively controlled in real-time to modify the flow field to provide an optimal cooling strategy to the whole battery pack.

A comparative parametric study among U-, Z-, and J-type structures is performed to further explore the sensitivities and effects of key system parameters, i.e., channel size, manifold configuration, charging/discharging rate, temperature, and cooling air flow rate. Based on the parametric analyses, a suite of key design parameters and constraints are determined to perform optimization. The grouped-channel optimizations of the three structures are performed using surrogate-based optimization. The pros and cons of the novel J-type structure are elaborated by comparing with the optimal U- and Z-type structures. A further J-type optimization regarding the manifold configuration is also conducted to show that the optimal settings of a BTMS vary with battery working conditions, and the J-type BTMS is capable of switching BTMS modes with controlling valves and air flow rate in real time to satisfy the cooling requirement. This study serves to develop a basic design concept of the J-type structure and to establish a pioneering foundation for further BTMS control or co-design framework.

The rest of the paper is organized as follows. Section 2 develops a battery electro-thermal model. Comparative studies on key design parameters of J-, Z-, and U-type BTMS are conducted in Section 3. In Section 4, grouped channels and manifold configurations are optimized using surrogate-based optimization, and the results are cross-validated with experiments. Concluding remarks and future work are discussed in the last section.

2. Battery electro-thermal model

2.1. Battery thermal model

It has been well studied that the volumetric heat generation rate of LIB is strongly influenced by the charging/discharging current, operating temperature, state of charge (SoC) [28], and cycles. A number of electrochemical/electrothermal models have been proposed in the literature to interpret the thermal mechanism. First proposed by Bernardi, then improved by Rao and Newman [29], a simplified LIB thermal model is expressed as

$$\dot{Q} = I(V - V_{oc}) + IT \frac{\partial V_{oc}}{\partial T} \quad (1)$$

where \dot{Q} represents the battery heat generation rate, V and V_{oc} denote the cell voltage and open circuit voltage, respectively. T is the battery cell operating average temperature, $\partial V_{oc}/\partial T$ is named as the entropic heat coefficient, and I is the battery current, which is defined as positive for charging and negative for discharging. The thermal model can be established by measuring the entropic heat coefficient. The first term is irreversible, mainly from the internal resistance ohmic losses, while the second term is reversible, known as the entropic heat from chemical reactions.

For simplification, the internal cell condition is assumed to be homogeneous, and the heat source derived above is assumed to be distributed uniformly inside the cell. Radiation heat transfer is neglected here since the temperature difference is limited. With these assumptions, the battery thermal behavior can be estimated using a lumped thermal model, as shown in Eq. (2).

$$mC_p \frac{\partial T}{\partial t} = \dot{Q} - hA(T_{cell} - T_{\infty}) \quad (2)$$

where m denotes the mass of battery cell, C_p is the average heat capacity, h represents the convective heat transfer coefficient, A is the effective surface area, and T_{∞} is the free stream temperature of the cooling media. This approach requires a precise measurement of the dynamic heat by using either the method of accelerating rate calorimeter (ARC) or isothermal heat conduction calorimeter (IHC).

2.2. Battery first order equivalent circuit model

Compared to the electrochemical model, an equivalent circuit model is more straightforward to characterize the relationship between battery electrical characteristics and its thermal behaviors. Fig. 1 shows the first order equivalent circuit, which consists of an ideal voltage source, an internal ohmic resistance, and a parallel RC circuit. The RC circuit is utilized here to interpret the dynamic response. All the parameters are contingent on the SoC, operating temperature, and battery cycle. The mathematical expression of the equivalent circuit is derived as follows:

$$v_t = V_{oc} - V_D - V_o + V_D e^{-\frac{t-t_0}{\tau}} \quad (3)$$

where $V_D = I \cdot R_D$ is the potential drop on the RC circuit, $V_o = I \cdot R_o$ is the potential drop on the internal resistance, and $\tau = R_D \cdot C_D$ denotes the time constant.

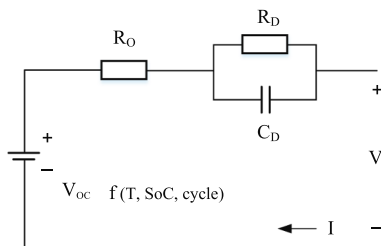


Fig. 1. First order equivalent circuit for LIB.

These parameters in Eq. (3) can be measured, extracted, and calculated with the method of hybrid pulse power characterization (HPPC) test [30,31]. In this study, Graphite/ $LiMn_2O_4$ pouch battery cells with a capacity of 1.6 Ah, and a nominal voltage of 3.75 V are used for experiments. A total of 200 groups of the characteristic data (R_o , R_D , and C_D) are extracted from various experimental settings. The heat generated by the resistances R_o and R_D is considered to be equal to the battery internal heat source. More details about the experiment setup, parameters analyses, and results validation can be found in Ref. [32]. The experimental data is then utilized to establish the battery electro-thermal model by using a surrogate model, which consists of three input variables: the current, SoC, and operating temperature.

2.3. Kriging approximation of battery electro-thermal model

After k-fold cross-validation, a Kriging approximation with second order polynomial regression and exponential error estimation is utilized to create a surrogate model based on the experimental data. A deterministic response $\mathcal{G}(I, SoC, T)$ with three dimensional variables is formulated with the Kriging surrogate model, given as

$$\mathcal{G}(I, SoC, T) = \mathcal{F}(\lambda, I, SoC, T) + \mathcal{R}(\omega, I, SoC, T) \quad (4)$$

where \mathcal{F} is defined as the regression model, and \mathcal{R} is the approximation error, given as

$$\mathcal{F}(\lambda, I, SoC, T) = f(I, SoC, T)\lambda \quad (5)$$

$$f(I, SoC, T) = [1, I_N, SoC_N, T_N, I_N^2, I_N SoC_N, I_N T_N, SoC_N^2, SoC_N T_N, T_N^2] \quad (6)$$

$$\mathcal{R}(\omega, I, SoC, T) = r(I, SoC, T)\omega \quad (7)$$

$$r(\gamma, I, SoC, T) = e^{(-\gamma|I-I_q|-\gamma_{SoC}|SoC-SoC_q|-\gamma_T|T-T_q|)} \quad (8)$$

where $f(I, SoC, T)$ denotes a vector of the normalized variables with orders 0, 1 and 2, in which the normalized variable is defined as $\alpha_N = (\alpha - \mu_\alpha)/\sigma_\alpha$, μ and σ are the mean and standard deviation, respectively. I_q , SoC_q , and T_q are the training data. All the Kriging parameters λ , ω , and γ are calculated by the generalized least squares estimation method [33,34].

Fig. 2 shows the equivalent volumetric heat generation rate distribution with respect to the operation current, SoC, and temperature. The electro-thermal model only covers the feasible operation ranges of current and temperature for LIB, and 10 A is suggested as the critical safety current. It indicates that decreasing the operating temperature tends to increase the internal resistance and thus induce a huge augment of heat generation rates. The calorific value is comparatively low around 60% SoC. Additionally, the overall battery thermal performance is more sensitive to the operating current than other parameters. This electro-thermal model can be applied to both charging and discharging

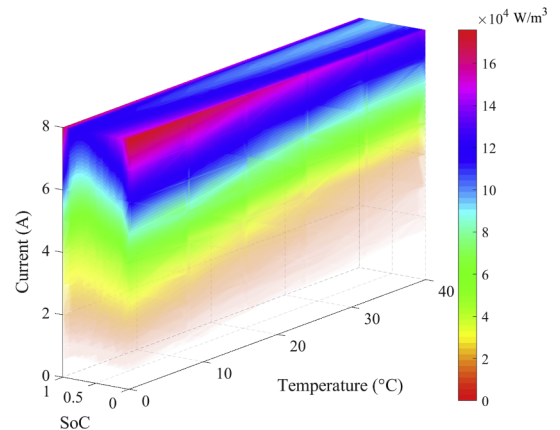


Fig. 2. The distribution of battery equivalent volumetric heat generation rate.

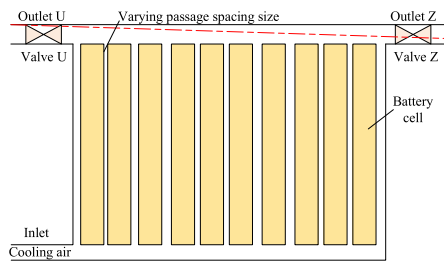


Fig. 3. The conceptual design of a J-type air-based BTMS.

conditions since the reversible heat is relatively smaller than the irreversible heat, especially under high current conditions.

3. Numerical parametric studies of air-based BTMS

3.1. Conceptual design of J-type BTMS

By taking the advantages of both *U*-type and *Z*-type air-based BTMS, this paper proposes a novel BTMS structure named *J*-type. A conceptual design of the *J*-type BTMS is illustrated in Fig. 3. The *J*-type BTMS prototype consists of ten battery cells with geometry sizes of 151 mm in height, 65 mm in length, and 16 mm in width based on Ref. [13].

As illustrated in Fig. 3, the size of channel and inlet manifold are first optimized under multiple working conditions, while the air flow rate and the openness of the two outlet valves will be adaptively controlled in real-time. By changing the air flow field via the openness of the two outlet valves, BTMS is able to cool down the hot area, thereby ensuring the temperature uniformity within a narrow range and improving the overall thermal performance. Moreover, the concept design is readily extended and applied to the battery pack level, since the concept module is arranged in a standard shape and can be extended from different directions.

The *J*-type BTMS can easily switch to *U*-type by completely closing the Valve *Z* and opening the Valve *U*, in which the front battery cells maintain a lower temperature than the rear ones. Similarly, the *J*-type BTMS can also switch to *Z*-type, by closing the Valve *U* and opening the Valve *Z*, which leads to better thermal performance for the rear battery cells. In between the two extreme conditions, the system can optimally adjust the opening degree of each valve based on the module temperature and battery working conditions.

To evaluate the effectiveness of the proposed *J*-type BTMS, a comparative study is performed among *J*-, *Z*-, and *U*-type BTMS. Three-dimensional (3D) CFD simulation models of the three types are built up in ANSYS Fluent with the *k*- ϵ (*k*- ϵ) turbulence model. The total size of the models converges to around 1,700,000 elements after grid dependence analysis, as shown in Fig. 4. The mass flow rate inlet and pressure outlet are selected as the inlet and outlet settings, respectively. The radiative heat transfer is neglected here due to the very limited temperature difference. The battery cell in the CFD model is assumed to have a uniform heat source and defined by a user-defined function, as derived in Section 2.3. A simulation takes approximately 25 min to converge on a six-core workstation.

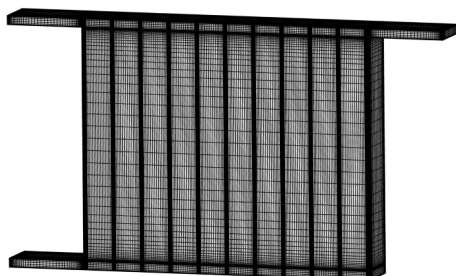


Fig. 4. The CFD meshing of J-type air-based BTMS.

A benchmark model with an even 3 mm channel size, an equal 6 mm inlet/outlet manifold size, and an initial inlet mass flow rate 7.1 g/s is set up for comparisons among the three types of BTMS. The initial temperature, discharging current, and SoC are set as 295 K, 3 C-rate, and 1, respectively, which correspond to a heat generation rate of 33,800 W/m³. The *J*-type outlet structure could be simplified into a tapered manifold for simulation convenience, as indicated by the dashed line in Fig. 3.

3.2. Effects of structure size

The BTMS structure uses three main parameters to define geometry size, i.e., channel interspacing size, collecting manifold size, and distribution manifold size. The numerical and experimental parametric studies of the *U*-type BTMS with respect to the channel size, equivalent heat generation rate, and mass flow rate have been well conducted in the authors' previous studies [35,20]. In this study, comparative parametric analyses among the three BTMS structures are performed to study and explore the sensitivity of BTMS to major design variables under certain conditions, so as to provide fundamental understandings for further BTMS optimization.

Fig. 5 shows the battery temperature distribution of *U*-type, *Z*-type, and *J*-type with different channel sizes. The curves represent the face-weighted average temperature of the battery pack. The maximum and minimum temperature of the same battery cell are represented by the upper bar and lower bar that are connected with vertical line segments, respectively. It is seen that the temperature distributions of *U*-type and *Z*-type are similar to each other, except that the distributions are opposite in terms of the maximum temperature location, in which the highest temperature of *U*-type occurs at the rear side, while the highest temperature of *Z*-type is located at the front side. The *J*-type's thermal performance is always better than the *U*- and *Z*-type structures, since it comprises an extra ventilation outlet. It also suggests that a narrow channel tends to uniformize the temperature distribution and lower the temperature rise simultaneously. However, as a side effect, a narrow channel may also lead to the augment of pressure drop and result in a higher pumping energy consumption, as shown in Fig. 6a. This is one of the most critical design considerations regarding maintenance and energy efficiency. Note that the parametric investigation mainly emphasizes on the ultimate thermal performance of the battery pack, though the mass flow rate and pressure drop vary from channel to channel.

Fig. 7 shows the relationship between the distribution manifold size and temperature rise. It is impressive that the 3 mm distribution manifold reduces and uniformizes the temperature distribution in both *U*- and *Z*-type. However, as shown in Fig. 6b, the 3 mm manifold almost triples in pressure drop compared to the benchmark cases, making it unsustainable in energy consumption. For *J*-type as shown in Fig. 7, increasing the size of the distribution manifold improves the thermal performance, and little difference is observed when the size is larger than 9 mm. Fig. 6b also indicates that the distribution manifold size for all three BTMS structures should be larger than 6 mm due to the significant augment of pressure drop.

In contrast to the distribution manifold, the collecting manifold performs differently, in particular with a small manifold size, as shown in Fig. 8. Under the benchmark flow rate condition, a 3 mm collecting manifold is too small for all the three structures, which results in unexpected high temperature (Fig. 8) and pressure drop (Fig. 6c). For the *U*-type BTMS, the 9 mm collecting manifold case performs the best regarding temperature rise and uniformity. For *Z*- and *J*-type, little discrepancy is observed when the collecting manifold is larger than 12 mm, which implies that enlarging the manifold size does not help to lower the temperature rise. Therefore, by analyzing Figs. 6–8, it is found that an appropriate manifold size ranges between 6 mm and 12 mm, which should also satisfy the constraints imposed by the entire battery pack volume and energy density.

3.3. Effects of controlled variables

Besides the structural parameters, controlled variables such as

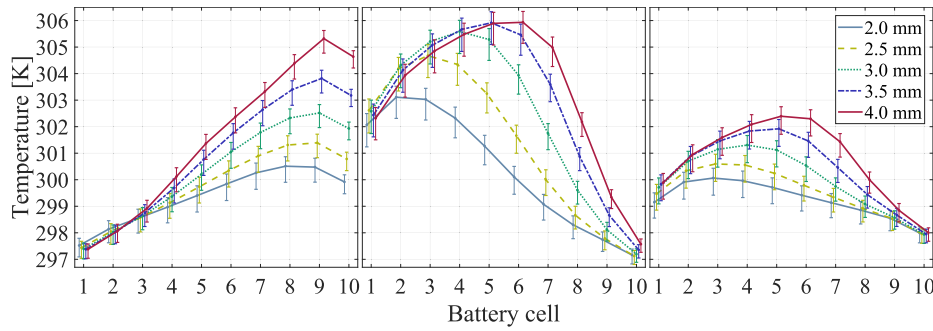


Fig. 5. Parametric analyses of channel size (From left to right: *U*-, *Z*-, and *J*-type).

operating temperature, heat generation rate, and air mass flow rate may also have strong influences on BTMS thermal performance. The Graphite/*LiMn₂O₄* battery is vulnerable to temperature, as discussed in Section 2.3. There is a closed-loop coupled relationship between the operating temperature and the battery heat generation rate, in which different operating temperature leads to varying heat generation rates, and thus impacts the battery pack temperature. For simplification, the SoC and battery current are fixed as 1 and 3 C-rate in simulations, respectively. Fig. 9 shows the effects of operating temperature on BTMS performance for *U*-, *Z*-, and *J*-type. It is seen that the temperature rise is significantly less in high-temperature environment than that of low-temperature environment, so does the temperature difference of the battery pack, since the internal resistance tends to decline in high-temperature environments.

As discussed in Section 2.3, there is a quadratic relationship between the battery equivalent heat generation rate and the charging/discharging current. To study the effects of operation current, the SoC and operating temperature are set as 1 and 295 K, respectively. The current investigation range is constrained between 1 C-rate and 3 C-rate, which equal to 3,700 and 33,800 W/m³ for heat generation rate, respectively. As seen from Fig. 10, the temperature rise presents a quasi-quadratic relationship with the C-rate current input. Both *U*- and *Z*-type deteriorate as the heat generation rate increases. The *J*-type has significant advantages over the other two types with high heat generation rates.

The impacts of cooling air mass flow rate on the BTMS performance are presented in Fig. 11. It shows that the temperature rise is approximately linear to the mass flow rate for both the *U*- and *J*-type BTMS. The only exception occurs at the rear side of *Z*-type: the temperature dose not change significantly as the mass flow rate increases, due to that most of the cooling air flows through the rear side channels.

3.4. Effects of modified structures

Extensive studies have been conducted in the literature, seeking to uniformly distribute the flow rate [36,37]. Specifically, the modified special structures with better fluid characteristics for BTMS can be

summarized into three types: uneven channels, tapered distribution manifold, and tapered collecting manifold. Fig. 12 shows the temperature distribution of priori grouped-channel cases, in which the benchmark cases (i.e., 3 mm even channels) are presented for comparisons. The channels are divided into three groups with combinations of every 4, 3, and 4 channels in different interspacing sizes. Note that the numbers in the legend (e.g., *U* 2-3-4) represents the sizes of grouped channels in mm, and *U* 3-3-3 denotes the benchmark case with even channels for the *U*-type BTMS. It is seen that all grouped-channel cases perform significantly better than the benchmark cases, where the temperature rise is reduced and the uniformity is also improved. The pressure drop is slightly increased for grouped-channel cases as shown in Fig. 13a.

Figs. 14 and 15 show the effects of tapered manifold modifications on the BTMS performance. The geometry of a tapered manifold is defined by the heights of two ends, as shown in the legend (e.g., 6–3 mm). The larger number represents the inlet size of the distribution manifold or the outlet size of the collecting manifold. Note that it is infeasible to have a smaller inlet for the distribution manifold or a smaller outlet for the collecting manifold in BTMS structure design, since it may generate back flows or eddies with extra vibration and noise inside the manifold. It is observed that the tapered distribution manifold (in Fig. 14) does not enhance the BTMS performance for *U*-type, while the tapered collecting manifold (in Fig. 15) has improved the uniformity and lowered the temperature rise for most cases. For the *J*-type BTMS with tapered manifolds, the tapered distribution manifold has improved the uniformity, while the tapered collecting manifold does not show a clear improvement. For *Z*-type, both the distribution and collecting tapered manifolds have improved the uniformity and lowered the temperature rise. The pressure drop is strongly affected by the manifold size, as illustrated in Fig. 13, and a structure with larger flow channels generally leads to less pressure drop. The overall impacts of modified structures are summarized in Table 1.

Based on the analyses performed above in this section, it is recognized that the geometry of the flow field, the channel size and the manifold configuration in particular, has a significant impact on the thermal performance and flow efficiency. The manifold configuration is

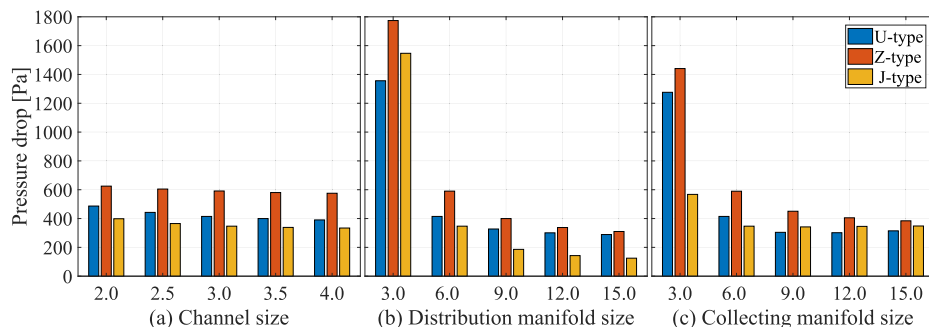


Fig. 6. The pressure drop of different structures with respect to different key parameters.

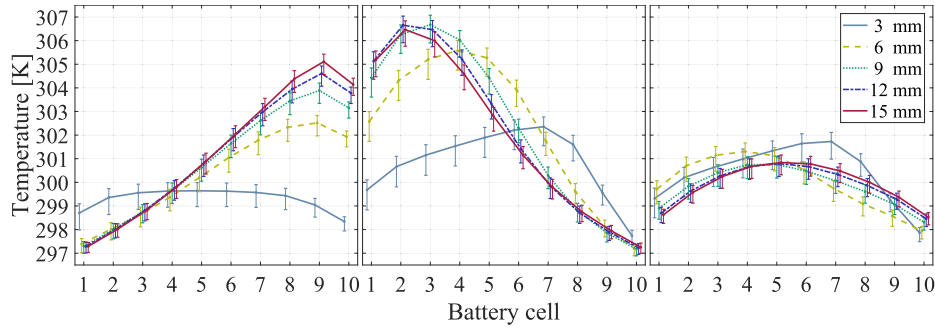


Fig. 7. Parametric analyses of distribution manifold spacing size (From left to right: U -, Z -, and J -type).

highly related to the pressure drop, and the appropriate size ranges between 6 mm and 12 mm. Not all of the priori optimized structures can surely enhance the performance. For example, the tapered distribution manifold does not improve the U -type performance, and so does the tapered collecting manifold for the J -type structure.

4. Surrogate-based optimization of air-based BTMS

Based on the parametric analyses above, it is recognized that the BTMS structure has remarkable influences on system performance. BTMS is a complex system, especially when considering modified structures and various working conditions, e.g., normal battery arrangement with time-dependent electric characteristics, uneven channels with tapered manifolds in steady stage, and J -type structure under real-time control conditions. To address the computational challenges in BTMS structure optimization with expensive CFD simulations, a surrogate-based optimization method is proposed in this study. The whole optimization is divided into two stages: Stage 1 optimizes the grouped-channel size for all three types (U , Z , and J), and Stage 2 further optimizes the distribution and collecting manifolds under different working conditions for the J -type BTMS.

4.1. Design of experiments

Three surrogate models are constructed based on a limited number of high fidelity CFD simulations of U -, Z -, and J -type BTMS. The optimal Latin Hypercube method is employed to perform a design of experiments (DoE) [38]. To set up CFD simulations, the 11 battery channels (as shown in Fig. 3) are divided into 4 groups with a layout of 3-3-2-3 channels from the front side to the rear side. The 4 grouped-channel sizes are considered as the design variables, ranging from 2 mm to 5 mm. The paralleled manifolds and other controlled variables remain the same as the benchmark case. A total of 50 simulations are conducted for each type, 75% of which are utilized as the training data, and the rest are treated as test data.

4.2. Surrogate modeling

An ensemble surrogate model is developed in this paper for BTMS modeling. A large pool of surrogate models is first constructed, which consists of 5 major groups with 62 surrogate models regarding different kernel functions or hyper parameters, e.g., Artificial Neural Network (ANN), Kriging/Gaussian Process Regression (GPR), Support Vector Machine (SVM), Radial Basis Functions (RBF), and Polynomial Response Surface (PRS). During the model training and selecting processes, a linear weighted evaluating criterion is adopted here to determine the appropriate models after K -fold cross-validation. Adopted criteria include the normalized maximum absolute error (NMAE) and normalized root mean square error (NRMSE), as given by:

$$NMAE = \frac{1}{n} \sum_{k=1}^n \frac{|\hat{y}_k - y_k|}{y_{max} - y_{min}} \quad (9)$$

$$NRMSE = \frac{1}{y_{max} - y_{min}} \sqrt{\frac{\sum_{k=1}^n (\hat{y}_k - y_k)^2}{n}} \quad (10)$$

where \hat{y} , y , y_{max} and y_{min} denote the corresponding estimated value, actual value, maximum value, and minimum value, respectively. n is the number of test data used in evaluating the performance.

Table 2 summarizes a subset of surrogate models with high accuracy from k -fold cross-validation. The surrogate models for the three types of BTMS have a similar level of accuracy, since they are all established based on fluid dynamics. However, the model accuracy decreases slightly from U -, Z - to J -type as the complexities of physical models increase. The weight factors of the ensemble surrogate model are solved using the least square method, and the hybrid model is given as:

$$Y_{hybrid} = \sum_{i=1}^{n_s} w_i \hat{y}_i \quad (11)$$

where w_i and \hat{y}_i are the weight factor and estimated value of i th surrogate, respectively. n_s denotes the number of ensemble surrogate members. Then a local impact factor β , defined as the ratio between the actual value and the hybrid model estimated value, is added based on

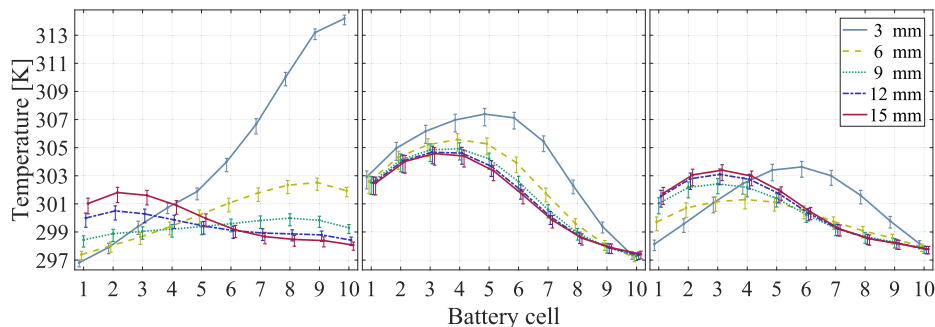


Fig. 8. Parametric analyses of collecting manifold spacing size (From left to right: U -, Z -, and J -type).

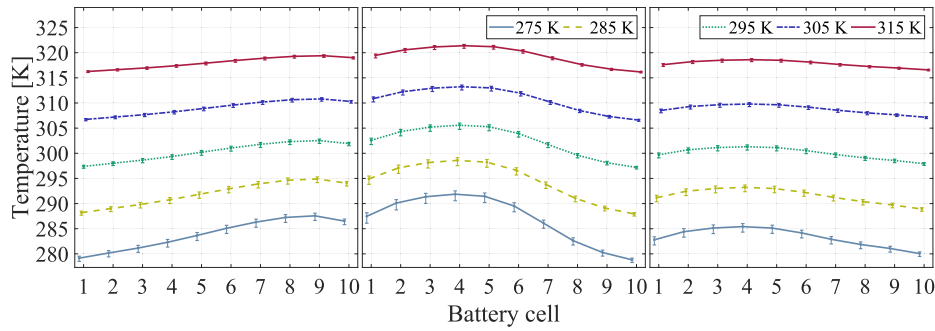


Fig. 9. Parametric analyses of operating temperature (From left to right: U -, Z -, and J -type)).

the methodology from the Extensive Adaptive Hybrid Function (E-AHF) in Ref. [39,40] to further tune surrogate estimates, as given in Eq. (12). This tuning step is only suggested for low-dimensional cases, since the uncertainty brought by high-dimensional features may worsen the hybrid surrogate estimation.

$$Y_{final} = \beta Y_{hybrid} \quad (12)$$

The surrogate estimation and error of the ensemble model and selected member models are shown in Fig. 16. Note that the ensemble model does not necessarily perform the best at every local estimation due to the high nonlinearity of the problem. However, the ensemble model captures the overall trend of the problem and provides the best global accuracy.

4.3. Optimization and adaptive sampling

The optimization objective is to minimize the maximum temperature $T_{max} = f(x_1, x_2, x_3, x_4)$, and the range of the grouped-channel size is considered as constraints. The optimization problem is formulated by:

$$\begin{aligned} \arg \min_x \quad & T_{max} = f(x_1, x_2, x_3, x_4) \\ \text{subject to} \quad & 2.0 \leq x_i \leq 5.0 \quad i = (1, 2, 3, 4) \end{aligned} \quad (13)$$

where $x_1 - x_4$ represent the grouped-channel size from the front to the rear side.

Our previous studies have also considered the total volume, temperature standard deviation, and pressure drop to perform a multi-objective optimization [21,41]. However, according to the parametric studies above, it is found that both the volume and pressure drop are highly related to the geometry size of the flow field. Once the mass flow rate and other controlled variables are fixed, the temperature uniformity is indirectly reflected by the maximum temperature. Though the parameters of pressure drop and temperature uniformity are not directly modeled in the objective function, they are still regarded as reference metrics to evaluate the BTMS performance.

The genetic algorithm (GA) is adopted here to perform the surrogate-based optimization. Fig. 17 shows the overall framework of surrogate-

based optimization and adaptive sampling. Here, a two-stage cluster sampling method is employed, in which the first stage is to cluster the candidate solutions, and the second stage is to generate adaptive samples using a Gaussian mixture model (GMM). The sampling probability is proportional to the size of clusters. The optimization and resampling process stops when the convergence criterion is met. After two rounds of resampling, as shown in Fig. 18, the resampling points converge to a small design region. The best sample among all the resampling data can be regarded as the optimum and the whole process terminates.

4.4. Optimization results

The optimal thermal management system of all three types are summarized in Table 3. Compared with the benchmark case, the optimized U -type has a 35.3% reduction in temperature rise, and a 63.4% improvement in temperature uniformity with a cost of 7.5% augment in pressure drop. Similarly for Z -type, the temperature rise and temperature standard deviation decrease by 46.6% and 69.1%, respectively, while the pressure drop increases by 5.0%. For J -type, the optimal arrangement has reduced the temperature by 31.18% and improved the uniformity by 67.8%, but increased the pressure drop by 12.7%.

Fig. 19 shows the CFD simulations of the three optimal designs. By comparing U - and Z -type structures, it is seen that the optimal maximum temperature of U -type is 21% lower than that of Z -type, but the pressure drop of U -type is 28% higher. Overall, U -type is more competitive in temperature-sensitive cases, while Z -type is more competitive in energy efficiency-sensitive cases. J -type has shown advantages in terms of both temperature and pressure drop. Due to the space occupied by the extra outlet, J -type is more suitable in volume-insensitive applications like HEV.

4.5. Manifold optimization of J -type BTMS

For the J -type BTMS as illustrated in Fig. 3, the system can optimally adjust the opening degree of the two valves based on the module temperature and the air mass flow rate. The openness degree of the two valves corresponds to the manifold size under a specific battery

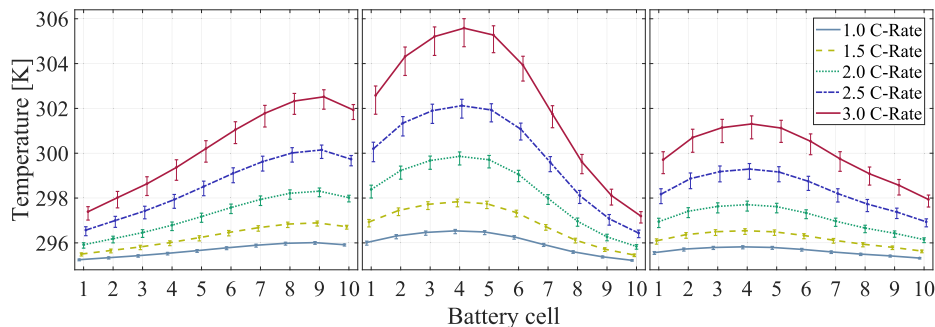


Fig. 10. Parametric analyses of charging/discharging current (From left to right: U -, Z -, and J -type)).

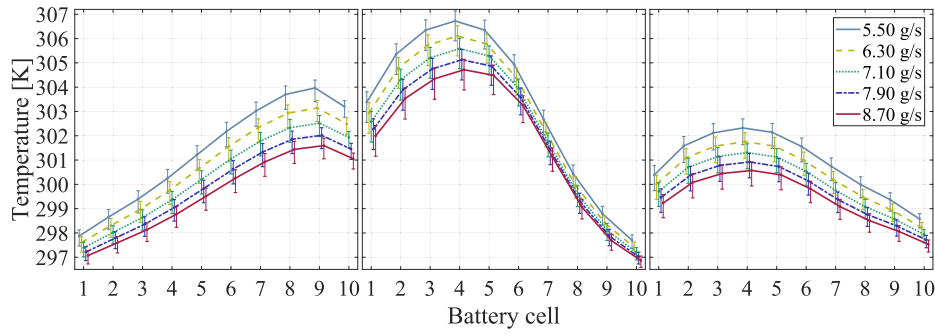


Fig. 11. Parametric analyses of mass flow rate (From left to right: *U*-, *Z*-, and *J*-type).

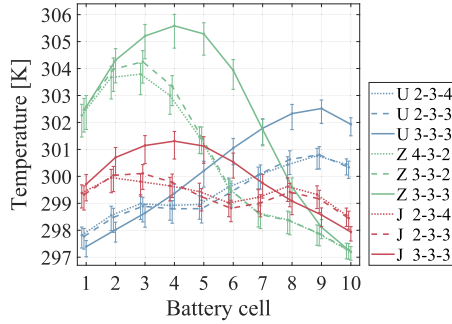


Fig. 12. Parametric analyses of grouped-channel sizes.

working condition. The goal of performing manifold optimization here is to validate the hypothesis that controlling the manifold size (via valves control) could further improve the thermal performance under varying working conditions. In this study, based on the optimal grouped-channel BTMS obtained from the previous optimization, a further step is performed to optimize the manifold under two working conditions.

The four manifold sizes are considered as the design variables, as shown in Fig. 20. The inlet of the distribution manifold is defined as $b_1 + b_2$ to prevent backflow. Similarly, the objective is to minimize the maximum temperature $T_{max} = f(b_1, b_2, b_3, b_4)$, given by:

$$\begin{aligned} \arg \min_b \quad & T_{max} = f(b_1, b_2, b_3, b_4) \\ \text{subject to} \quad & 0 \leq b_1 \leq 9 \\ & 3 \leq b_2 \leq 7 \\ & 0.5 \leq b_3 \leq 15 \\ & 0.5 \leq b_4 \leq 15 \end{aligned} \quad (14)$$

The optimizations are performed under two different working conditions: (1) the benchmark condition, and (2) the comparative condition that has double heat generation rate and double air flow rate compared to the benchmark condition. A number of surrogate models are also constructed here using the same surrogate modeling method

discussed in Section 4.2, and the performances are shown in Fig. 21. The entire process terminates after two rounds of resampling and optimization. Fig. 22 shows the optimization and resampling results under both the benchmark and comparative conditions. It is seen that the resampling under the comparative condition is not as concentrated as the benchmark condition due to accuracy difference.

Table 4 highlights the optimal configuration results under the two conditions. By comparison, the optimal manifold configuration varies between the benchmark and the comparative conditions. Thus, the optimal setting of BTMS changes with battery working condition, and an air-based BTMS with a fixed structure is unable to always work in its optimal settings under changing working conditions. The proposed *J*-type cooling system has introduced more flexibility with two controlling valves. Coupled with its optimal control strategy, the *J*-type system is capable to adapt itself to the changing conditions.

4.6. Experimental validation

An experimental platform is established to study the thermal performance of different pure-air based BTMS, in which different types of BTMS can be shifted flexibly. As shown in Fig. 23, the platform consists of three parts, i.e., the air and power supply section, the battery model section, and the measurement section. The equivalent heat source of the battery cell is replaced with two heaters, which are controlled by the DC power source. The detailed settings of the platform can be found in Ref. [35]. Several groups of experiments are performed to mutually validate the benchmark and optimized cases.

Fig. 24 compares the simulation and experimental temperature distributions for both the benchmark and optimal cases. There are only small discrepancies observed between simulations and experiments, which is mainly attributed to the settings of temperature measuring position. The maximum temperature in experiments is measured by a K type thermocouple that is inserted deep inside the top part of an aluminum model cell, while the maximum temperature is directly extracted from the lateral surface in simulations. Other potential factors such as measurement accuracy, initial condition settings, the bias of grouped-channel size, and CFD turbulence model, may also contribute

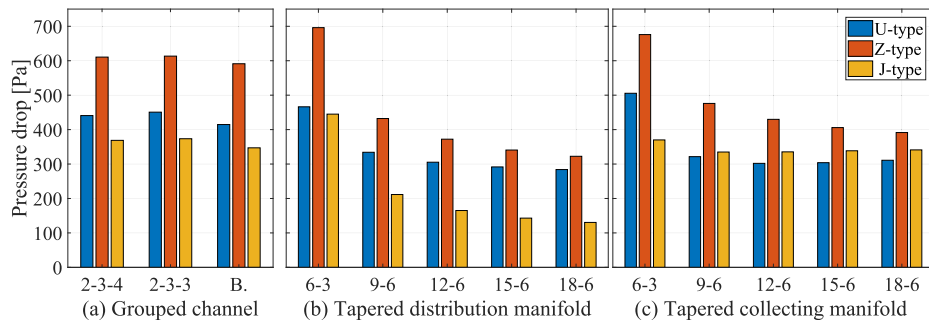


Fig. 13. The pressure drop of different modified structures (B.:Benchmark cases).

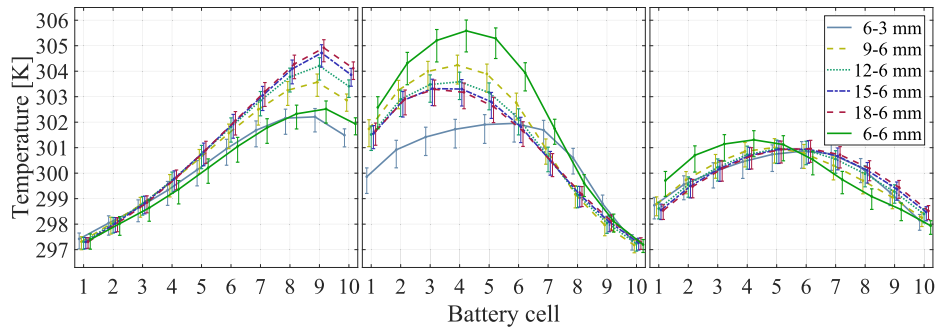


Fig. 14. Parametric analyses of tapered distribution manifold size (From left to right: *U*-, *Z*-, and *J*-type).

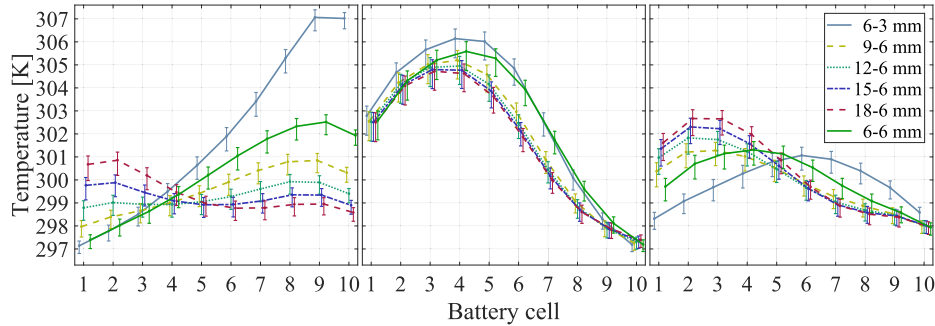


Fig. 15. Parametric analyses of tapered collecting manifold size (From left to right: *U*-, *Z*-, and *J*-type).

Table 1
Summary of the modified structures.

| Improvement (Y/N) | <i>U</i> -type | <i>Z</i> -type | <i>J</i> -type |
|-------------------------------|----------------|----------------|----------------|
| Grouped Channels | Y | Y | Y |
| Tapered Distribution Manifold | N | Y | Y |
| Tapered Collecting Manifold | Y | Y | N |

Table 2
Evaluation results of a subset of surrogate models (Note: Bold values indicate the smallest errors).

| Model-Kernel | <i>U</i> -type | | <i>Z</i> -type | | <i>J</i> -type | |
|-----------------|----------------|-------------|----------------|-------------|----------------|-------------|
| | NMAE | NRMSE | NMAE | NRMSE | NMAE | NRMSE |
| RBF-TPS | 2.47 | 4.39 | 4.92 | 7.99 | 4.37 | 5.94 |
| GPR-Matern32 | 2.49 | 4.09 | 3.49 | 5.60 | 4.11 | 5.57 |
| RBF-Cubic | 2.50 | 4.14 | 4.32 | 6.64 | 4.14 | 5.40 |
| GPR-Ardmatern32 | 2.58 | 4.29 | 3.31 | 4.98 | 3.97 | 5.23 |
| SVR-Polynomial | 2.71 | 4.03 | 4.54 | 6.56 | 5.31 | 7.59 |
| PRS-Cubic | 2.87 | 4.09 | 4.64 | 7.11 | 4.27 | 5.59 |
| KRG-Poly2gauss | 3.01 | 4.62 | 4.61 | 6.67 | 4.73 | 6.41 |
| SVR-RBF | 3.02 | 4.26 | 4.54 | 7.92 | 5.38 | 7.12 |
| ANN-RBFN | 3.57 | 6.03 | 3.35 | 6.50 | 5.04 | 7.24 |

to the small differences between simulations and experiments. Overall, the experiment results agree with the simulation results, which further validates the parametric analysis and optimization results in this study.

5. Conclusion

This paper proposed a novel *J*-type air-based battery thermal management system by integrating the conventional *U*-type and *Z*-type structures. An electro-thermal model for Lithium-ion battery was developed, based on which a comparative parametric study of several structural and controlled variables was performed. It is recognized that the geometry of the flow field has a significant impact on thermal

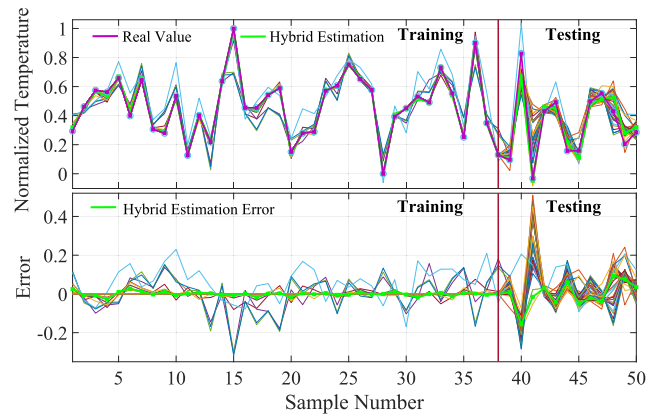


Fig. 16. Surrogate model estimation and error from both ensemble and individual member models for *J*-type.

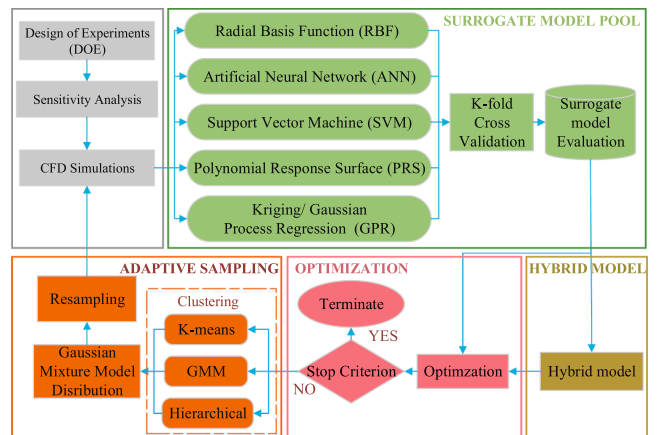


Fig. 17. The overall framework of adaptive surrogated-based optimization for BTMS.

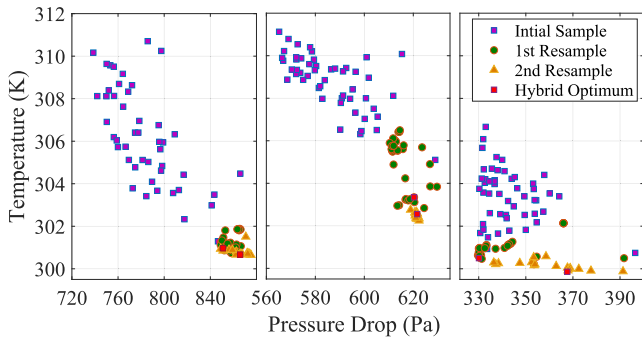


Fig. 18. The optimization and resampling results (From left to right: *U*-, *Z*-, and *J*-type).

performance and flow efficiency. Several priori optimized structures like grouped-channel and tapered manifold were also investigated to develop fundamental understandings for further optimization. Results showed that the tapered distribution manifold brings no improvements to the *U*-type structure, and so does the tapered collecting manifold to the *J*-type structure.

A surrogate-based optimization was performed to improve the grouped-channel structures for *U*-, *Z*-, and *J*-type battery thermal management system, in which the Gaussian mixed model resampling method was adopted to improve the accuracy. The optimal results showed that there were 35.3%, 46.6%, and 31.18% reduction in the temperature rise for *U*-, *Z*-, and *J*-type, respectively. A *J*-type manifold configuration optimization was also performed to further explore the optimal settings of the system under different working conditions. It demonstrated that the optimal settings of *J*-type structure vary across the working conditions, and the *J*-type system is able to be adaptively

Table 3
The optimal designs of *U*-, *Z*-, and *J*-type BTMS.

| Type | Design Variable (mm) | | | | Evaluation Criteria | | | | | |
|---------------------|----------------------|-------|-------|-------|---------------------|------------|----------|--------------|----------------|-------------------|
| | x_1 | x_2 | x_3 | x_4 | $T_{max}(K)$ | ΔT | $T_G(K)$ | ΔT_G | $\Delta P(Pa)$ | $\Delta \Delta P$ |
| <i>U</i> -Benchmark | 3 | 3 | 3 | 3 | 303.75 | - | 2.30 | - | 801.48 | - |
| <i>U</i> -Optimum | 2.01 | 2.14 | 2.81 | 3.86 | 300.66 | -35.3% | 0.84 | -63.4% | 862.20 | 7.50% |
| <i>Z</i> -Benchmark | 3 | 3 | 3 | 3 | 308.41 | - | 4.11 | - | 592.70 | - |
| <i>Z</i> -Optimum | 4.96 | 2.51 | 2.14 | 2.01 | 302.16 | -46.6% | 1.27 | -69.1% | 622.34 | 5.0% |
| <i>J</i> -Benchmark | 3 | 3 | 3 | 3 | 302.15 | - | 1.43 | - | 347.25 | - |
| <i>J</i> -Optimum | 2.74 | 2.66 | 2.13 | 2.02 | 299.98 | -31.18% | 0.46 | -67.8% | 391.28 | 12.7 % |

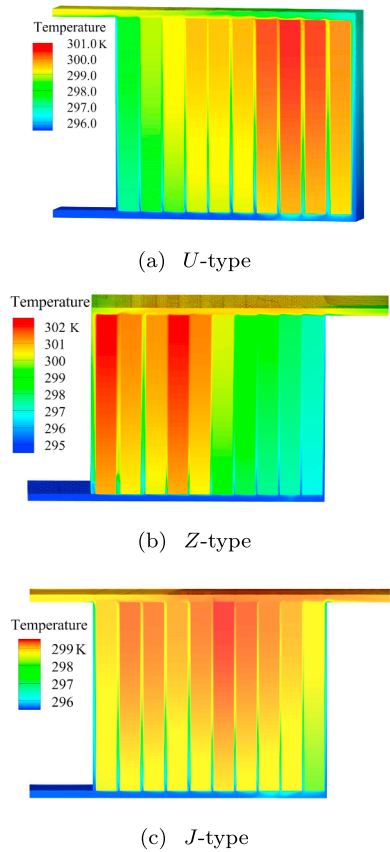


Fig. 19. CFD simulation results of the optimal designs of *U*-, *Z*-, and *J*-type BTMS.

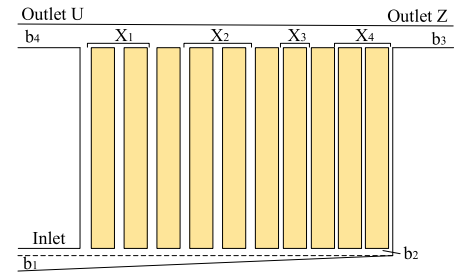


Fig. 20. The second stage optimization of *J*-type BTMS.

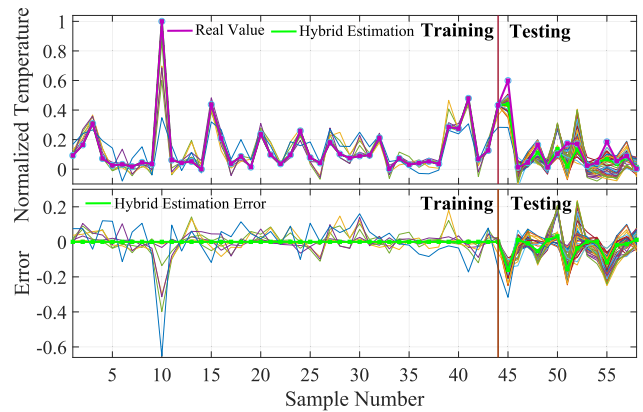


Fig. 21. Surrogate model evaluations of *J*-type under the benchmark condition.

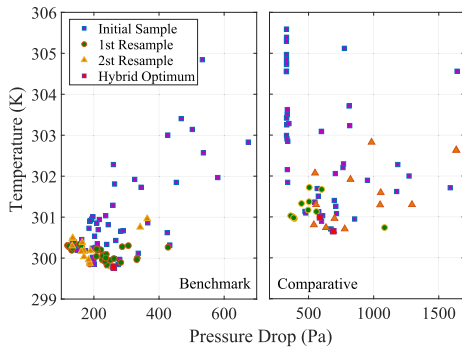


Fig. 22. The *J*-type manifold optimization process for the benchmark and comparative conditions.

controlled to the optimal settings by adjusting the two valves. The simulations and optimizations were further verified by experiments.

This study serves to develop a basic concept of the *J*-type cooling system. For the *J*-type structure, the temperature uniformity can be significantly enhanced by switching the working mode between *U*- and *Z*-type alternately, which is controlled by the opening degree of the two valves. Potential future work will develop an optimal control strategy under dynamic driving conditions. Moreover, the structure size of the battery pack will also be optimized by using a co-design framework.

Acknowledgments

The authors would like to thank Prof. Babak Fahimi and Dr. Zhuo Yang, at the Department of Electrical and Computer Engineering, The University of Texas at Dallas, for providing data on battery electro-thermal modeling.

Table 4
The *J*-type optimized results under different conditions

| Types | Design Variable (mm) | | | | Benchmark condition | | | Comparative condition | | |
|-------------------|----------------------|-------|-------|-------|---------------------|-----------|-----------------|-----------------------|-----------|-----------------|
| | b_1 | b_2 | b_3 | b_4 | T_{max} (K) | T_c (K) | ΔP (Pa) | T_{max} (K) | T_c (K) | ΔP (Pa) |
| <i>J</i> -stage1 | 0 | 6.0 | 6.0 | 6.0 | 299.98 | 0.46 | 391.28 | 301.9 | 0.86 | 1,233.3 |
| <i>J</i> -stage2B | 1.28 | 6.05 | 13.62 | 8.23 | 299.78 | 0.28 | 260.8 | 301.56 | 0.75 | 894.25 |
| <i>J</i> -stage2C | 2.5 | 6.55 | 11.31 | 10 | 300.1 | 0.37 | 261.9 | 300.66 | 0.34 | 690.4 |

J-stage1: optimal case in Stage 1 optimization.
J-stage2B: optimal case in Stage 2 optimization under the benchmark condition.
J-stage2C: optimal case in Stage 2 optimization under the comparative condition.
 (Note: Bold values indicate the best results).

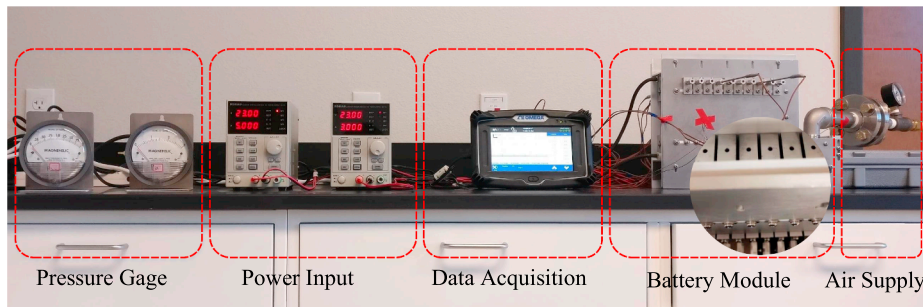


Fig. 23. The air-based BTMS experimental platform.

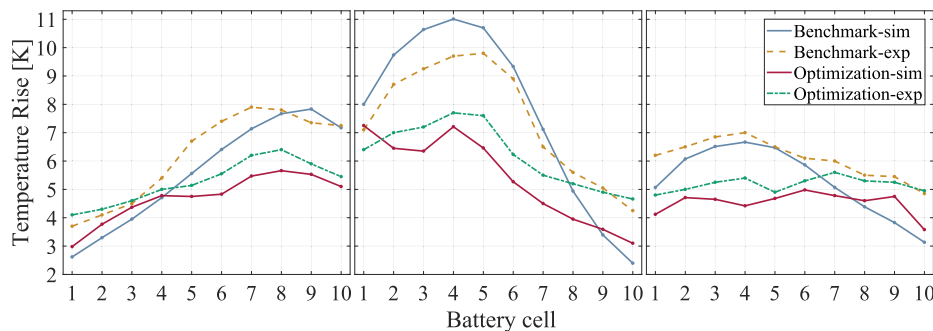


Fig. 24. Comparing results between simulations and experiments (From left to right: *U*-, *Z*-, and *J*-type).

- change material. *Int J Hydrogen Energy* 2014;39(8):3904–13.
- [24] Ling Z, Chen J, Fang X, Zhang Z, Xu T, Gao X, et al. Experimental and numerical investigation of the application of phase change materials in a simulative power batteries thermal management system. *Appl Energy* 2014;121:104–13.
- [25] Lazrak A, Fourmigué J-F, Robin J-F. An innovative practical battery thermal management system based on phase change materials: numerical and experimental investigations. *Appl Therm Eng* 2018;128:20–32.
- [26] Ling Z, Wang F, Fang X, Gao X, Zhang Z. A hybrid thermal management system for lithium ion batteries combining phase change materials with forced-air cooling. *Appl Energy* 2015;148:403–9.
- [27] Burban G, Ayel V, Alexandre A, Lagonotte P, Bertin Y, Romestant C. Experimental investigation of a pulsating heat pipe for hybrid vehicle applications. *Appl Therm Eng* 2013;50(1):94–103.
- [28] Alfi A, Charkhgard M, Zarif MH. Hybrid state of charge estimation for lithium-ion batteries: design and implementation. *IET Power Electron* 2014;7(11):2758–64.
- [29] Rao L, Newman J. Heat-generation rate and general energy balance for insertion battery systems. *J Electrochem Soc* 1997;144(8):2697–704.
- [30] Yang Z, Patil D, Fahimi B. Online estimation of capacity fade and power fade of lithium-ion batteries based on input-output response technique. *IEEE Trans Transport Electrification* 2018;4(1):147–56.
- [31] He H, Xiong R, Guo H. Online estimation of model parameters and state-of-charge of LiFePo4 batteries in electric vehicles. *Appl Energy* 2012;89(1):413–20.
- [32] Yang Z, Patil D, Fahimi B. Electrothermal modeling of lithium-ion batteries for electric vehicles. *IEEE Trans Vehic Technol* 2019;68(1):170–9.
- [33] Lophaven S, Nielsen H, Sondergaard J. Dace a matlab kriging toolbox [eb/ol]; 2016.
- [34] Cui M, Zhang J. Estimating ramping requirements with solar-friendly flexible ramping product in multi-timescale power system operations. *Appl Energy* 2018;225:27–41.
- [35] Liu Y, Li M, Zhang J. An experimental parametric study of air-based battery thermal management system for electric vehicles. In: ASME 2017 international design engineering technical conferences and computers and information in engineering conference, American Society of Mechanical Engineers; 2017. p. V02AT03A024–V02AT03A024.
- [36] Bassiouny M, Martin H. Flow distribution and pressure drop in plate heat exchangers-i u-type arrangement. *Chem Eng Sci* 1984;39(4):693–700.
- [37] Wang J. Pressure drop and flow distribution in parallel-channel configurations of fuel cells: Z-type arrangement. *Int J Hydrogen Energy* 2010;35(11):5498–509.
- [38] Söbester A, Leary SJ, Keane AJ. A parallel updating scheme for approximating and optimizing high fidelity computer simulations. *Struct Multidiscip Optim* 2004;27(5):371–83.
- [39] Zhang J, Chowdhury S, Messac A. An adaptive hybrid surrogate model. *Struct Multidiscip Optim* 2012;46(2):223–38.
- [40] Song X, Lv L, Li J, Sun W, Zhang J. An advanced and robust ensemble surrogate model: extended adaptive hybrid functions. *J Mech Des* 2018;140(4):041402.
- [41] Liu Y, Ghassemi P, Chowdhury S. J. Zhang, Surrogate based multi-objective optimization of j-type battery thermal management system. In: ASME 2018 international design engineering technical conferences and computers and information in engineering conference, American Society of Mechanical Engineers; 2018. p. V02BT03A034–V02BT03A034.